Available online at www.sciencedirect.com
SCIENCE DIRECT®
Comput. Methods Appl. Mech. Engrg. 194 (2005) 935–956
Computer methods in applied mechanics and engineering
www.elsevier.com/locate/cma

Boundary element analysis of three-dimensional mixed-mode cracks via the interaction integral

A.P. Cisilino *, J. Ortiz

Welding and Fracture Division, INTEMA, Faculty of Engineering, University of Mar del Plata—CONICET, Av. Juan B. Justo 4302, Mar del Plata 7600, Argentina

Received 28 February 2003; received in revised form 30 July 2003; accepted 5 August 2003

Abstract

A three-dimensional boundary element method (BEM) implementation of the interaction integral methodology for the numerical analysis of mixed-mode three-dimensional cracks is presented in this paper. The interaction integral is evaluated from a domain representation naturally compatible with the BEM, since stresses, strains and derivatives of displacements at internal points can be evaluated using their appropriate boundary integral equations. Special emphasis is put in the selection of the auxiliary function that represents the virtual crack advance in the domain integral. This is found to be a key feature to obtain reliable results at the intersection of crack fronts with free surfaces. Several examples are analysed to demonstrate the efficiency and accuracy of the implementation.

Keywords: Fracture mechanics; Energy domain integral; Interaction integral; Boundary elements

1. Introduction

Evaluation of fracture parameters is usually the purpose of carrying out a numerical model of a crack problem. Two-dimensional analyses are usually sufficient to characterize through-thickness cracks. However, part through cracks, which are the most common type of crack defect found in service conditions, have an inherently three-dimensional character. The solution to three-dimensional crack problems can

* Corresponding author. Tel.: +54 223 4816600; fax: +54 223 4810046.
E-mail address: cisilino@fi.mdp.edu.ar (A.P. Cisilino).

0045-7825/$ - see front matter
doi:10.1016/j.cma.2003.08.014

be obtained by such techniques us the finite element method (FEM) and the boundary element method (BEM).

When the basic assumption of linear elastic fracture mechanics is adopted, the stress intensity factors can be evaluated in FEM and BEM by a variety of techniques, such us the extrapolation of displacements or stresses, special crack tip elements, the virtual crack extension method, the subtraction of singularity technique, the alternating method and J-integral methods [1,2]. Techniques based on the extrapolation of displacements an stresses are easy to implement, but they present the drawback that a very high level of mesh refinement is required for its accurate evaluation [2], what makes them computationally expensive. Similarly, alternating and virtual crack extension methods are also computationally expensive, as they require of multiple computer runs to solve the problem. On the other hand, J-integral methods, being an energy approach, eliminate the need to solve local crack tip fields accurately, since if integration domains are defined over a relatively large portion of the mesh, accurate modelling of the crack tip is unnecessary because the contribution to J of the crack tip fields is not significant. The J-integral as devised by Rice [3] characterizes the crack driving force for two-dimensional problems, therefore for general three-dimensional cases involving cracks of arbitrary shape an alternative form for J is needed. Three basic schemes have evolved for the numerical computation of the J-integral in three dimensions: virtual crack extension methods [4,5], generalization of Rice's contour integral [6] and domain integral methods [7–9].

The BEM is ideally suited for the evaluation of path independent integrals, since the required stresses, strains and derivatives of displacements at internal points can be directly obtained from their boundary integral representations. It also has been shown that BEM produces more accurate stresses and strains at internal points when compared with other numerical techniques, and therefore better results can be achieved. The application of the BEM for the evaluation of J-integral in three-dimensional problems have been the reported by Rigby and Aliabadi [10], Huber and Kuhn [11], Cisilino et al. [12,13] and dell'Erba and Aliabadi [14]. Although the bulk of fracture mechanics literature is concerned with the first mode of crack deformation, there are practical engineering problems that involve mixed-mode conditions. Of the above cited papers, the works by Rigby [10] and dell'Erba [14] proposed methods for decoupling the J-integral for mixed-mode cracks in which the symmetric and antisymmetric parts of the displacement, strain and stress fields are separated.

Among the available methods for calculating fracture parameters, the energy domain integral (EDI) has shown well suited for three-dimensional BEM analysis [12,13]. The EDI is versatile, efficient and relatively simple to implement numerically. To develop the domain integral the EDI incorporates an auxiliary function q, which can be interpreted as a virtual crack front advance. This makes the EDI similar to the virtual crack extension technique [15,16] but has the advantage that only one computer run is necessary to evaluate the point wise energy release rate along the complete crack front. On the other hand, the interaction or M_1-integral methodology originally proposed by Chen and Shield [17] has emerged as an efficient methodology for decoupling the J-integral for mixed-mode cracks. The M_1-integral methodology is based on the superposition of two equilibrium states, given by the actual problem and a set of auxiliary known solutions. The M_1-integral methodology has been implemented using BEM for two-dimensional cracks by Miyazaki et al. [18].

This work presents a BEM domain formulation of the M_1-integral for the computation of mixed-mode stress intensity factors along three-dimensional crack fronts. The domain representation of the interaction integral is presented in a straightforward approach, together with the details of its BEM implementation. Special emphasis is put in the appropriate selection of the auxiliary function q, which was found to be a key feature to obtain reliable results at the intersection of crack fronts with free surfaces. Several examples are analysed to demonstrate the efficiency and accuracy of the implementation.

2. The energy domain integral

Consider a three-dimensional crack front with a continuously turning tangent as depicted in Fig. 1(a). Define a local coordinate system x^* at position η, where the crack energy release rate is evaluated, given by x_1^* normal to the crack front, x_2^* normal to the crack plane, and x_3^* tangent to the crack front.

Following Natha and Moran [16], the general crack-tip contour integral along three-dimensional crack front takes the form

$$I(\eta) = \lim_{C\to 0} \delta l(\eta) \int_{C(\eta)} \left(w \cdot \delta_{ki} - \sigma_{ij}^* u_{j,k}^* \right) n_i \, \mathrm{d}C, \tag{1}$$

where w is the strain energy density, σ_{ij}^* and $u_{j,k}^*$ are Cartesian components of stress and displacement derivatives expressed in the local system x^*, $\delta l(\eta)$ is the local crack extension, n_i is the unit vector normal to the contour C (which lies in the $x_1^* - x_2^*$ plane), and $\mathrm{d}C(\eta)$ is the differential of the arc length C (see Fig. 1(a)). It is worth noting that, although Eq. (1) comes from two-dimensional analysis it applies for three-dimensional case, as in the limit as $C \to 0$, plain strain conditions prevail so that the three-dimensional fields approach the plane problem.

In order to derive the equivalent domain representation of Eq. (1), we consider a small segment L_c of the crack front that lies in the local $x_1^* - x_3^*$ plane as shown in Fig. 1(b). Next we assume that the segment undergoes a virtual crack advance in the plane of the crack, and we define the magnitude of the advance at each point η as $\Delta a(\eta)$. We note that $\Delta a(\eta)$ varies continuously along $\delta\eta$ and vanishes at each end of the segment. Now let

$$\overline{I} = \int_{L_c} I(\eta) \Delta a(\eta) \, \mathrm{d}\eta, \tag{2}$$

where $I(\eta)$ is the integral defined in Eq. (1). When $I(\eta)$ belongs to the point-wise energy release rate, I gives the total energy released when the finite segment L_c undergoes the virtual crack advance.

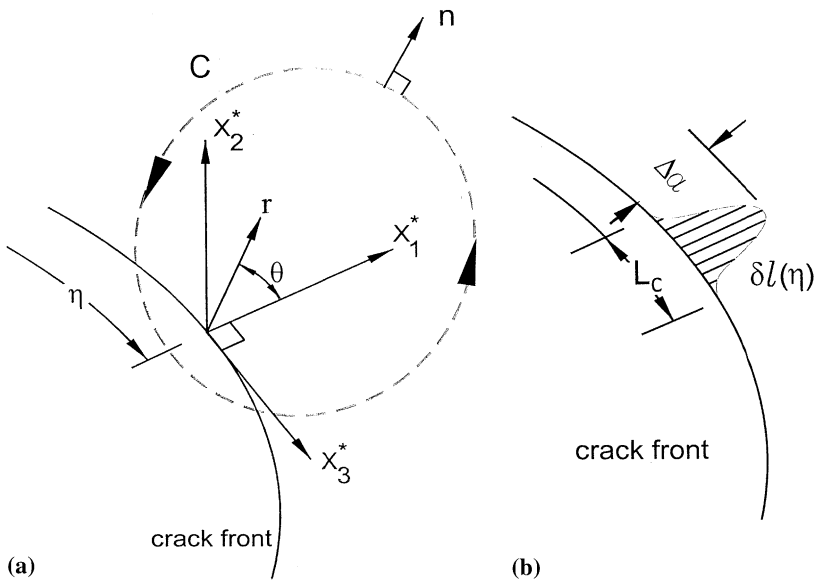

Fig. 1. (a) Definition of the local orthogonal Cartesian coordinates at point η on the crack front. (b) Virtual crack front advance.

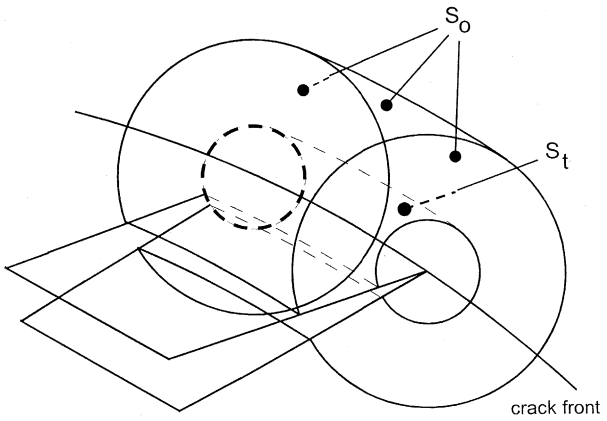

Fig. 2. Tubular domain surrounding a segment of the crack front.

The appropriate domain form of the pointwise crack-tip contour integral can be obtained from Eq. (2) by considering a tubular domain V surrounding the crack segment as shown in Fig. 2. As shown in the figure, the surface S_t is formed by translating the contour C along the segment L_c, and S_o stands for the outer surface of V including the ends. Next an auxiliary function q is introduced, which is sufficiently smooth in V and it is defined on the surfaces of V as follows:

$$q = \begin{cases} \Delta a \cdot \delta l(\eta) & \text{on } S_t, \\ 0 & \text{on } S_o. \end{cases} \tag{3}$$

Finally, in the limit as the tubular surface S_t is shrunk onto the crack segment L_c; in the absence of crack face tractions, we obtain the domain integral

$$I = \int_V \left(\sigma_{ij}^* u_{j,k}^* - w\delta_{ki}\right) q_{,i} \, \mathrm{d}V. \tag{4}$$

In the evaluation of the energy release rate, in the absence of body forces the integral given by Eq. (4) reduces to the domain representation of the familiar J-integral. A simple relationship between $J(\eta)$ and the pointwise crack-tip integral $I(\eta)$ can be obtained if it is assumed that $I(\eta)$ is constant along the segment L_c. It follows directly from Eq. (2) that

$$J(\eta) = \frac{\overline{I}}{\int_{L_c} \Delta a(\eta) \, \mathrm{d}\eta}. \tag{5}$$

3. The interaction integral

In this section, the interaction or M_1-integral methodology for decoupling three-dimensional mixed-mode stress intensity factors is presented. The M_1-integral is based on the principle of superposition. Let us consider two equilibrium states with field variables denoted by the superscripts (1) and (2), respectively. Superposition of the two equilibrium states leads to another one, (1 + 2). Then the stress intensity factors $K_j^{(1+2)}$ can be written as

$$K_j^{(1+2)} = K_j^{(1)} + K_j^{(2)} \quad (j = \mathrm{I,II,III}). \tag{6}$$

The stress intensity factors can be related to the J-integral in a plain strain condition as follows:

$$J = J_{\mathrm{I}} + J_{\mathrm{II}} + J_{\mathrm{III}} = \frac{1}{E}(K_{\mathrm{I}}^2 + K_{\mathrm{II}}^2) + \frac{K_{\mathrm{III}}^2}{2\mu}, \tag{7}$$

where E is the Young's and μ is the shear modulus. Using Eq. (7), the J-integral for the superimposed state (1 + 2) can be written as

$$J^{(1+2)} = \frac{1}{E}\left[\left(K_{\mathrm{I}}^{(1+2)}\right)^2 + \left(K_{\mathrm{II}}^{(1+2)}\right)^2\right] + \frac{\left(K_{\mathrm{III}}^{(1+2)}\right)^2}{2\mu} = J^{(1)} + J^{(2)} + \frac{2}{E}(K_{\mathrm{I}}^{(1)}K_{\mathrm{I}}^{(2)} + K_{\mathrm{II}}^{(1)}K_{\mathrm{II}}^{(2)}) + \frac{K_{\mathrm{III}}^{(1)}K_{\mathrm{III}}^{(2)}}{\mu}. \tag{8}$$

Then, the M_1-integral is defined as

$$\frac{2}{E}(K_{\mathrm{I}}^{(1)}K_{\mathrm{I}}^{(2)} + K_{\mathrm{II}}^{(1)}K_{\mathrm{II}}^{(2)}) + \frac{K_{\mathrm{III}}^{(1)}K_{\mathrm{III}}^{(2)}}{\mu} = J^{(1+2)} - J^{(1)} - J^{(2)} = M_1. \tag{9}$$

Using Eq. (4) a domain representation of the M_1-integral can be obtained as follows:

$$M_1 = \int_V \left(\sigma_{ij}^{*(1)}u_{j,k}^{*(2)} + \sigma_{ij}^{*(2)}u_{j,k}^{*(1)} - \sigma_{ij}^{*(1)}\varepsilon_{ij}^{*(2)}\delta_{ki}\right)q_{k,i}\,\mathrm{d}V. \tag{10}$$

For the decoupling the mixed-mode stress intensity factors the problem under consideration is selected as equilibrium state (1), so that the field variables $\sigma_{ij}^{*(1)}$ and $u_{j,k}^{*(1)}$ will be obtained in this work from the results of a boundary element analysis. On the other hand, the well-known plain-strain solutions for the asymptotic crack-tip fields with prescribed stress intensity factors K_{I}, K_{II} and K_{III}, are selected as the equilibrium state (2). Then the field variables related with the equilibrium state (2), $\sigma_{ij}^{*(2)}$, $u_{j,k}^{*(2)}$ and $\varepsilon_{ij}^{*(2)}$ are calculated from these asymptotic solutions. Finally the M_1-integral defined in Eq. (10) can be calculated, using the field variables related with the equilibrium states (1) and (2). By using three sets of asymptotic solutions, $(K_{\mathrm{I}}^{(2)} = 1, K_{\mathrm{II}}^{(2)} = 0, K_{\mathrm{III}}^{(2)} = 0)$, $(K_{\mathrm{I}}^{(2)} = 0, K_{\mathrm{II}}^{(2)} = 1, K_{\mathrm{III}}^{(2)} = 0)$ and $(K_{\mathrm{I}}^{(2)} = 0, K_{\mathrm{II}}^{(2)} = 0, K_{\mathrm{III}}^{(2)} = 1)$, it is possible to obtain the stress intensity factor solutions for individual modes from Eq. (9) as follows:

$$K_{\mathrm{I}}^{(1)} = \frac{M_1^a \cdot E}{2} \quad K_{\mathrm{II}}^{(1)} = \frac{M_1^b \cdot E}{2} \quad K_{\mathrm{III}}^{(1)} = M_1^c \cdot \mu, \tag{11}$$

where M_1^a, M_1^b and M_1^c are the values of the M_1-integral calculated using the three sets of asymptotic solutions.

It is important to point out that the present implementation of the M_1-integral approach is only valid for straight crack fronts. For the application of the M_1-integral along curved crack fronts extra terms need to be included in Eq. (10) [19]. It is also worth noting that since the M_1-integral is based upon the assumption that the near-crack tip fields asymptote to the plane strain fields, it is not strictly applicable at the intersection of the crack front with a free surface. It turns that out that at the intersection of the crack front and a free surface, the singularity is more severe than the usual $1/\sqrt{r}$ singularity. The performance of the proposed methodology at the intersection of the crack front with a free surface is extensively discussed in the following sections of the paper.

4. The dual boundary element method and modeling considerations

Although the conventional BEM is efficient in carrying out general stress analysis, it is not possible to use it directly for general mixed mode crack problems. The coincidence of the crack surfaces make the

collocation point on two surfaces identical, leading to a mathematical generation [1]. Among the special techniques devised to overcome this difficulty the dual boundary element method (DBEM) is the more general and versatile. In what follows the DBEM is briefly presented following Cisilino et al. [20,21]. The reader is referred to the cited references for further details.

The dual boundary integral equations on which the DBEM is based are the displacement and the traction integral equations. Considering a body with domain $\Omega(X)$ surrounded by a boundary $\Gamma(x)$, the displacement boundary integral equation relating the boundary displacements $u_j(x)$ with the boundary tractions $t_j(x)$ can be written as,

$$C_{ij}(x')u_i(x') + \int_\Gamma T^*_{ij}(x',x)u_j(x)\,\mathrm{d}\Gamma(x) = \int_\Gamma U^*_{ij}(x',x)t_j(x)\,\mathrm{d}\Gamma(x), \tag{12}$$

where i, j denote Cartesian components; and $T^*_{ij}(x',x)$ and $U^*_{ij}(x',x)$ represent the Kelvin traction and displacement fundamental solutions at a boundary point x due to a unit load placed at location x'.

Assuming continuity of both strains and tractions at x' on a smooth boundary, the boundary traction integral equation is obtained by differentiating Eq. (12) and applying the material constitutive relationships

$$\frac{1}{2}t_i(x') + n_i(x')\int_\Gamma T^*_{ijk}(x',x)u_k(x)\,\mathrm{d}\Gamma(x) = n_i(x')\int_\Gamma U^*_{ijk}(x',x)t_k(x)\,\mathrm{d}\Gamma(x), \tag{13}$$

where $n_i(x')$ denotes the component of the outward unit normal to the boundary at x'. The kernels $T^*_{ijk}(x',x)$ and $U^*_{ijk}(x',x)$ contain derivatives of $T^*_{ij}(x',x)$ and $U^*_{ij}(x',x)$ together with elastic constants.

The above formulation can be rewritten in terms of the crack opening and sliding displacements to reduce the number of unknowns (see Aliabadi and Rooke [1]). Considering that the model boundary Γ can be divided into three surfaces: Γ^+ and Γ^-, which are the two coincident crack surfaces, and Γ^e, which is the remaining surfaces, the displacement and traction equations (12) and (13) can be re-written for the case of traction-free crack surfaces using a simplified notation as

$$C_{ij}(x')u_i(x') + \int_{\Gamma^e} T^*_{ij}u_j\,\mathrm{d}\Gamma + \int_{\Gamma^+} T^*_{ij}\Delta u_j\,\mathrm{d}\Gamma = \int_{\Gamma^e} U^*_{ij}t_j\,\mathrm{d}\Gamma, \tag{14}$$

$$\frac{1}{2}t_i(x') + n_i(x')\int_{\Gamma^e} T^*_{ijk}u_k\,\mathrm{d}\Gamma + n_i(x')\int_{\Gamma^+} T^*_{ijk}\Delta u_k\,\mathrm{d}\Gamma = n_i(x')\int_{\Gamma^e} U^*_{ijk}t_k\,\mathrm{d}\Gamma, \tag{15}$$

where the new unknowns are given by the relative displacement between the crack faces $\Delta u_j = u_j^+ - u_j^-$.

The general modelling strategy can be summarized as follows:

- only one of the crack surfaces is discretized and the traction boundary integral equation (15) is applied for collocation. The discretization is done using discontinuous elements, which are used to fulfill the continuity requirements of the field variables for the existence of the traction equation,
- continuous elements are used over the remaining model boundary, except at the intersection of the crack with the boundary surface. In this region edge discontinuous elements are employed to avoid common nodes at the intersection. The displacement boundary integral equation (14) is used to collocate in both cases.

This simple strategy is robust and allows the DBEM to effectively model general crack problems. Crack tips, crack edge corners and crack kinks do not require special treatment, since they are not located at nodal points where the collocation is carried out.

5. Stresses, strains and displacement derivatives

5.1. Internal points

As it has been stated in Section 3, the application of the M_1-integral methodology requires the stress and displacement derivative fields σ^*_{ij} and $u^*_{j,k}$ to be known within the integration volume V. Although this quantities must be expressed in the local crack-front coordinate system x^*, in this work, and for the sake of simplicity, they will be firstly computed in the global system x and later transformed to the local system x^*. Bearing this into mind, and in order to integrate the computation of the M_1-integral into the DBEM formulation, derivatives of the displacements at internal points X' are obtained from their boundary integral representations. The integral equation for the displacement derivatives results from the analytical differentiation of the internal counterpart of Eq. (13):

$$u_{i,m}(X') = \int_{\Gamma^e} U^*_{ij,m} t_j \,\mathrm{d}\Gamma - \int_{\Gamma^e} T^*_{ij,m} u_j \,\mathrm{d}\Gamma - \int_{\Gamma^+} T^*_{ij,m} \Delta u_j \,\mathrm{d}\Gamma, \tag{16}$$

where the terms $U^*_{ij,m}$ and $T^*_{ij,m}$ are the derivatives of the fundamental displacement U^*_{ij}, and traction T^*_{ij} solutions.

Once the displacement derivatives $u_{j,k}$ are known, stresses σ_{ij} and strains ε_{ij} can be computed using the basic continuum mechanics relationships:

$$\varepsilon_{i,j} = \tfrac{1}{2}(u_{i,j} + u_{j,i}), \tag{17}$$

$$\sigma_{ij} = 2\mu\varepsilon_{ij} + \frac{2\mu v}{1-2v}\varepsilon_{kk}\delta_{ij}. \tag{18}$$

5.2. Boundary points

Displacement partial derivatives $u_{i,m}$ at boundary nodes could be obtained from Eq. (14), in a similar way to their internal counterparts, by taking the limit of Eq. (14) as point X' moves to the boundary, i.e. $X' \to x'$. However, this procedure is computationally expensive because of the occurrence of hypersingular integrands. To avoid this difficulty, stresses and strains, as well as the displacements on the model surface are evaluated in this work from the boundary displacements and tractions. Consider with this purpose a local Cartesian system, x^0_1, x^0_2, x^0_3, such that x^0_3 is the unit vector in the normal direction to the boundary element. If u^0_j, ε^0_{ij}, σ^0_{ij} and t^0_j are the displacements, strains, stresses and tractions in the local system, stress components in the normal direction can be written as

$$\sigma^0_{i3} = t^0_i. \tag{19}$$

The remaining stress tensor components, σ^0_{11}, σ^0_{12} and σ^0_{22} can be expressed in terms of t^0_3 and the tangential strain tensor components ε^0_{11}, ε^0_{22} and ε^0_{12} by eliminating ε^0_{33} from the general expression of Hooke's law. Thus,

$$\begin{aligned}
\sigma^0_{11} &= \frac{1}{1-v}\left[v t^0_3 + 2\mu\left(\varepsilon^0_{11} + v\varepsilon^0_{22}\right)\right],\\
\sigma^0_{22} &= \frac{1}{1-v}\left[v t^0_3 + 2\mu\left(\varepsilon^0_{22} + v\varepsilon^0_{11}\right)\right],\\
\sigma^0_{12} &= 2\mu\varepsilon^0_{12}.
\end{aligned} \tag{20}$$

Strain components ε^0_{ij} can be found using Eq. (17), now applied in the local coordinate system.

It is worth nothing that displacement derivatives in Eq. (17) are initially evaluated in the intrinsic element directions (ξ_1, ξ_2) and then converted to the local coordinate system x^0, since as usual in BEM, boundary displacements are given in terms of the piecewise parametric representation (shape functions) of intrinsic coordinates.

Finally, the nine components of the partial displacement derivatives $u^*_{j,m}$ are computed. Using chain differentiation, derivatives of the displacements in the global system $u_{j,m}$, are related to the derivatives of the displacements with respect to the intrinsic boundary element directions $\partial u_i/\partial\xi_j$ as follows

$$\frac{\partial u_i}{\partial \xi_j} = \frac{\partial u_i}{\partial x_k}\frac{\partial x_k}{\partial \xi_j}, \tag{21}$$

where $\partial x_k/\partial\xi_j$ is the Jacobian matrix of the transformation.

As it can be seen, Eq. (21), once expanded, yields a set of six equations with the nine derivatives $u_{i,k}$ as unknowns. Three of these unknowns $u_{1,1}$, $u_{2,2}$, $u_{3,3}$, can be directly calculated from the strain tensor components ε_{11}, ε_{22} and ε_{33}, respectively by using Eq. (17). This leaves the system with six unknowns, which can be further reduced to three if the values of ε_{12}, ε_{13} and ε_{23} are substituted in Eq. (17) and then replaced in the system of equations. Finally, the three remaining unknowns are calculated using a set of three equations taken from the system generated by Eq. (21). It is worth noting that, since one or more of the derivatives $\partial u_k/\partial\xi_j$ can become simultaneously zero depending on the element orientation and shape, the selection of the three equations cannot be arbitrary, being necessary to make special selection in each case.

6. Boundary element implementation

6.1. Interaction integral evaluation

The computation of the M_1-integral was included in the DBEM code as a post-processing procedure, and so it could be applied to the results from a particular model at a later stage. As it has been stated in Section 3, Eq. (11) allows computation of the mixed-mode stress intensity factors at any position η on the crack front. In each case, this requires the evaluation of a volume integral within closed domains that enclose a segment of the crack front L_c. A natural choice here is to make η coincident with the element nodes on the crack front, while L_c is taken as the element or element sides at which points η lies (see Fig. 3).

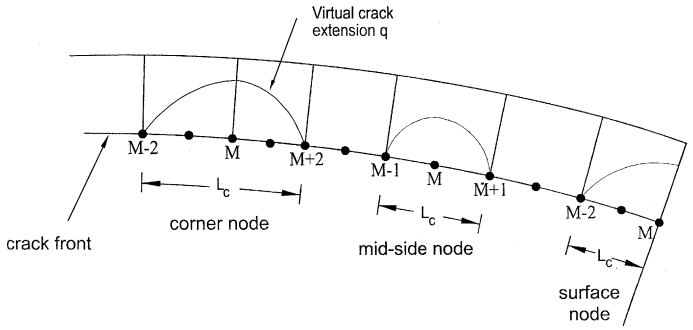

Fig. 3. Schematic of the volume cells in the crack front region illustrating the virtual crack extensions for a corner node, a mid-node and a surface node.

The portion of the model domain in which the volume integrals are evaluated is discretized using 27-noded isoparametric (brick) cells, over which stresses, strains and displacements derivatives are approximated by products of the cell interpolation functions Φ_i and the nodal values of σ_{ij}, ε_{ij} and $u_{i,j}$. Nodal values of these variables are computed following the procedures introduced in Sections 5.1 and 5.2 depending on whether the node is internal or lies on the model boundary. Volume discretization is designed to have a web-style geometry around the crack front, while the integration volumes are taken to coincide with the different rings of cells. This is illustrated in Fig. 4, where one of the model faces has been removed to show the crack and the integration domains.

As depicted in Fig. 3, three different cases need to be considered, depending on whether the node of interest M is in the middle of an element side (mid-node), it is shared by two elements (corner node), or it is located coincident with the external surface (surface node). If the node M is a mid-node or surface node, L_c (the segment of the crack front over which the M_1-integral is computed) spans over one element, connecting nodes $M-1$, M, and $M+1$ and nodes $M-2$, $M-1$ and M, respectively. On the other hand, if M is a corner node, L_c spans over two elements, connecting nodes from $M-2$ to $M+2$.

Function q is specified at all nodes within the integration volumes. Consistent with the isoparametric formulation, these q-values are given by

$$q = \sum_{i=1}^{27} \phi_i Q^i, \tag{22}$$

where Φ_i are the shape functions defined within each volume cell and Q^i are the nodal values for the ith node. From the definition of q (see Eq. (3)), $Q^i = 0$ if the ith node is on S_0, while for nodes inside V, Q^i are given by interpolating between the nodal values on L_c and S_0. Different criteria for specifying Q^i are discussed in next section.

Following standard manipulations

$$q_{,j} = \sum_{i=1}^{27} \sum_{k=1}^{3} \frac{\partial \phi_i}{\partial \zeta_k} \frac{\partial \zeta_k}{\partial x_j} Q^i, \tag{23}$$

where ζ_k are the coordinates in the cell isoparametric space.

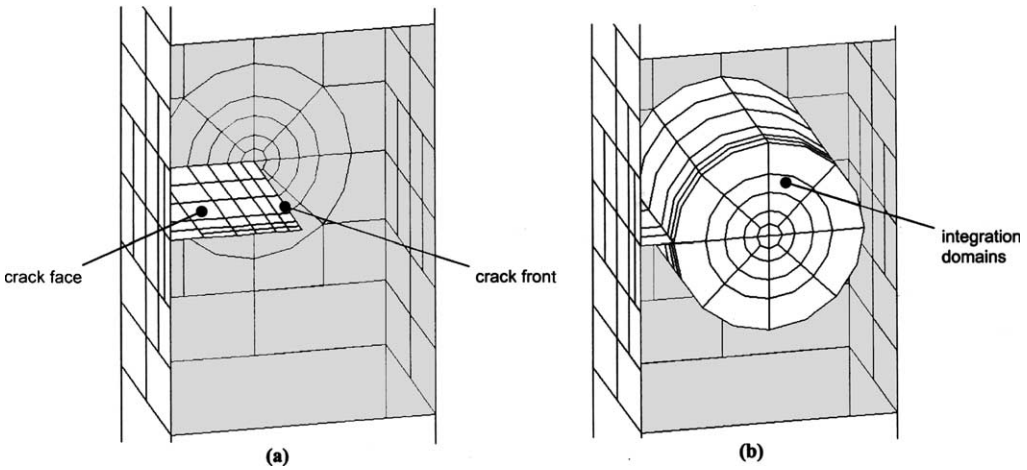

Fig. 4. Boundary element discretization and integration cells.

If Gaussian integration is used, the discretized form of Eq. (10) is given by

$$M_1 = \sum_{\text{cells in } V} \sum_{p=1}^{m} \left\{ \left(\sigma_{ij}^{*(1)} u_{j,k}^{*(2)} + \sigma_{ij}^{*(2)} u_{j,k}^{*(1)} - \sigma_{ij}^{*(1)} \varepsilon_{ij}^{*(2)} \delta_{ki} \right) q_{,i} \det \left(\frac{\partial x_j}{\partial \xi_k} \right) \right\}_p w_p, \tag{24}$$

where m is the number of Gaussian points per cell, and w_p are the weighting factors.

6.2. The q-function

The auxiliary function q was introduced in Section 2 in order to model the virtual crack front advance. Since the virtual crack advance can adopt any arbitrary shape, the only requirement for function q is to be sufficiently smooth within the integration volume V as the evaluation of the EDI requires of its differentiation.

Shih et al. [22] have shown that for the EDI the computed value of J is insensitive to the assumed shape of the q function. However, it has been found in this work that the shape of the function q is relevant for the performance of M_1-integral computations. In this sense two different approaches for the shape of function q are investigated.

6.2.1. Bi-quadratic q

This definition of q has been employed with excellent results in the computation of EDI in a previous work by one of the authors [12]. Within this approach q is defined to vary quadratically in the directions tangential and normal to the crack front. Considering that the evaluation point η is at the middle of the crack front segment L_c, and r_0 is the radius of the integration domain, the function q is written as:

$$q(x^*) = \left\| 1 - \left(\frac{x_3^*}{L_c/2} \right)^2 \right\| \cdot \left[1 - \left(\frac{r}{r_0} \right)^2 \right], \tag{25}$$

where r is the distance from the crack front in the $x_1^* - x_2^*$ plane as depicted in Fig. 1.

6.2.2. Optimised q

In a recent paper Saliva et al. [9] proposed an optimum shape for the function q which under certain considerations ensures the convergence of the EDI computations. The proposed function is

$$q(x^*) = \frac{W^p \|x^*\|^{-\beta}}{W^p \|x^*\|^{-\beta} + \sum_{i=1}^{N} W_j^{np} \|x^* - z_i\|^{-\beta}}, \tag{26}$$

where w^p, w^{np}, and β are parameters to be chosen, and z_i, are the positions of the N points with null prescribed values of q. These are given in this work by the N cell-nodes located on S_o, the outer surface of the integration volume V.

Using parameters w^p, w^{np}, and β, it is possible to control which parts of the domain significantly contribute to the integral (see Eqs. (4) and (10)). In particular β is associated with the smoothness of q. Greater values induce approximately null gradients around the crack front, where non-null values of q are prescribed. In contrast, the field undergoes abrupt changes outside these regions. With w^p and w^{np}, the region with non-null gradients can be translated near the crack front or near the boundary of the integration volume where null values of q are prescribed. Fig. 5 illustrates the influence of the parameters as function of r/r_0.

Finally, it is worth to mention that although Saliva et al. [9] propose specifying the value of q independently of any mesh, in this work the q-values are interpolated using the internal cell shape functions as it has been presented in Section 6.1.

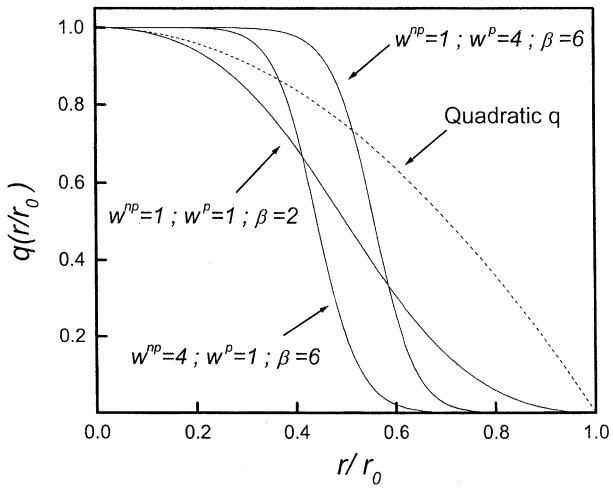

Fig. 5. Influence of parameters w^p, w^{np}, and β on the shape of function q (one dimensional case).

7. Examples

7.1. Thick centre-cracked and double-edge-notched specimens

In order to start with the validation of the proposed formulation two examples under pure Mode-I solicitation are chosen as first examples. They are a thick centre-cracked panel (CCP) and a double-edge-notched specimen (DENS) subjected to a uniaxial remote tension σ. Both examples are analysed using the same base geometry, to which appropriate boundary conditions are applied in each case as illustrated in Fig. 6. Also depicted in Fig. 6 are the model dimensions that were chosen to coincide with those used by

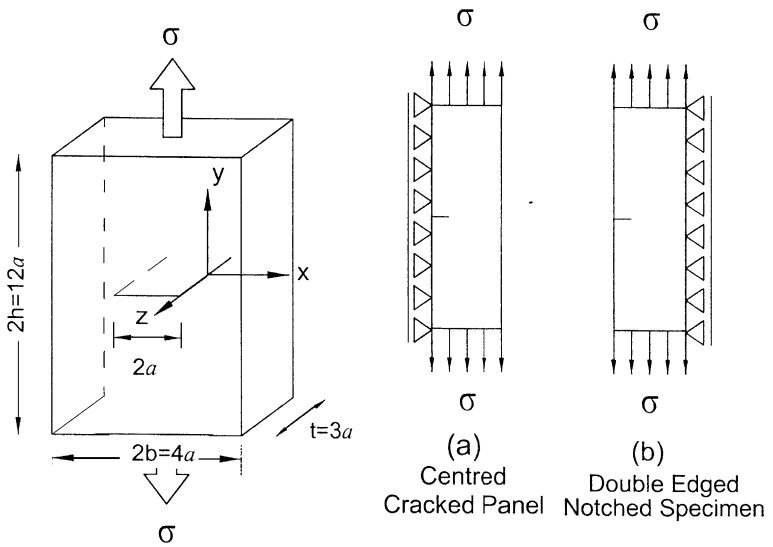

Fig. 6. Geometry and dimensions of CCP and DENS.

Raju and Newman [23] for the sake comparison. Material properties are Young's modulus $E = 1000$ N/mm^2 and Poisson ratio $\nu = 0.33$.

Model discretization is depicted in Fig. 4. It consists of 193 elements and 1040 nodes. Six elements are placed along the crack front, and a total of 35 elements are used in the crack discretization. Crack front element dimensions are graded towards the free surface, being the smallest equal to $t/32$. Four rings of cells with radii r/a equal to 0.2, 0.35, 0.5 and 0.75 are accommodated around the crack front for K computations. With this purpose 216 cells and 2262 modes are employed.

K_I-values were computed using the two approaches introduced in Section 6 for the specification of q. Normalized results obtained for the CCP using the bi-quadratic function q are given in Table 1, while results obtained using the optimised q are presented in Table 2. Following Saliva et al. [9] parameter values for the optimised q are chosen as $w^p = 6$, $w^{np} = 1$, and $\beta = 6$. Both sets of results are plotted in Fig. 7, together with the reference values from Ref. [23]. Error bars indicate the 5% accuracy of the reference values.

Excellent agreement is found between the reported and computed results using both approaches for q, except for the point coincident with the free surface, $z/t = 0.5$, where the optimised q performs markedly better. It can also be observed from Table 1 that the K_I-values computed at the free surface present a strong dependence with the integration volume. If in any way an average value is computed using these results, the resulting value presents almost 40% error with respect to the reference. On the other hand, the K_I-value obtained using the optimised q is almost independent of the integration volume, and it has only a 3% deviation with respect to the reference. Finally, it is worth to mention that with the only exception of the K_I-value obtained using the bi-quadratic q for the point located on the free surface, all the other results present a deviation less than 3% with respect to reference. Note that this deviation is always smaller than the 5% accuracy reported for the reference.

Results for the DENS are plotted Fig. 8, together with the reference values from Ref. [23]. Results show the same behaviour than for the CCP. For interior points results obtained using the bi-quadratic and the optimised q are very accurate, while only the optimised q allows obtaining an accurate result at the free surface.

7.2. Thick panel with a centre slant crack

This second example includes a crack under mixed load conditions. It consists in a thick panel with a centre slant crack rotated $\theta = 30°$ with respect to the horizontal, and subjected to a uniaxial remote ten-

Table 1
Normalized $K_I/\sigma\sqrt{\pi a}$ results for the CCP specimen using the bi-quadratic q

z/t	$K_I/\sigma\sqrt{\pi a}$						
	r/a				Average	Ref. [23]	Diff. %
	0.20	0.35	0.50	0.75			
0.0000	1.2012	1.2063	1.2090	1.2104	1.2067	1.197	0.81
0.0625	1.1970	1.2038	1.2079	1.2106	1.2048	1.201	0.32
0.1250	1.2027	1.2098	1.2134	1.2157	1.2104	1.206	0.36
0.1875	1.2055	1.2133	1.2178	1.2209	1.2144	1.211	0.28
0.2500	1.2194	1.2270	1.2307	1.2331	1.2276	1.214	1.12
0.3125	1.2316	1.2410	1.2458	1.2489	1.2418	1.223	1.54
0.3750	1.2387	1.2467	1.2503	1.2528	1.2471	1.232	1.23
0.4063	1.2435	1.2489	1.2507	1.2519	1.2487	1.237	0.96
0.4375	1.2508	1.2575	1.2597	1.2613	1.2573	1.244	1.07
0.4531	1.2549	1.2615	1.2636	1.2659	1.2615	1.245	1.33
0.4688	1.2401	1.2467	1.2485	1.2499	1.2463	1.235	0.91
0.4844	1.2142	1.2199	1.2206	1.2198	1.2186	1.198	1.72
0.5000	0.9489	0.7725	0.6115	0.3767	0.6774	1.102	38.53

Table 2
Normalized $K_I/\sigma\sqrt{\pi a}$ results for the CCP specimen using the optimised q

z/t	$K_I/\sigma\sqrt{\pi a}$						
	r/a				Average	Ref. [23]	Diff. %
	0.20	0.35	0.50	0.75			
0.0000	1.2121	1.2047	1.2075	1.2094	1.2084	1.197	0.95
0.0625	1.2092	1.2049	1.2051	1.2051	1.2061	1.201	0.42
0.1250	1.1993	1.2085	1.2090	1.2089	1.2064	1.206	0.03
0.1875	1.2117	1.2119	1.2121	1.2121	1.2120	1.211	0.08
0.2500	1.2188	1.2237	1.2241	1.2238	1.2226	1.214	0.99
0.3125	1.2372	1.2385	1.2387	1.2387	1.2383	1.223	1.25
0.3750	1.2424	1.2518	1.2522	1.2523	1.2497	1.232	1.44
0.4063	1.2199	1.2206	1.2206	1.2206	1.2204	1.237	−1.34
0.4375	1.2400	1.2456	1.2457	1.2457	1.2443	1.244	0.02
0.4531	1.2296	1.2296	1.2296	1.2296	1.2296	1.245	1.24
0.4688	1.2096	1.2103	1.2102	1.2102	1.2101	1.235	2.01
0.4844	1.1768	1.1768	1.1768	1.1768	1.1768	1.198	−1.77
0.5000	1.0785	1.0667	1.0660	1.0659	1.0693	1.102	−2.97

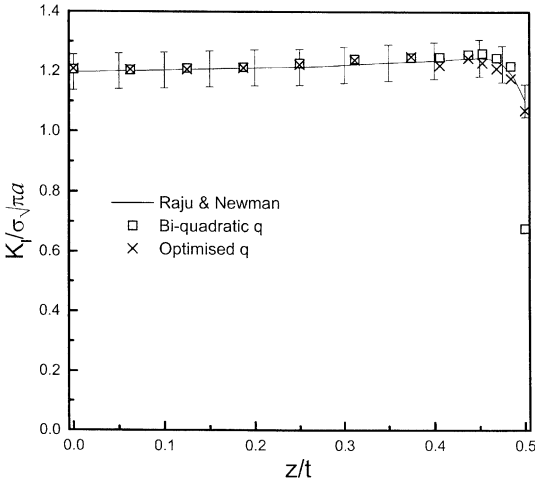

Fig. 7. Variation of $K_I/\sigma\sqrt{\pi a}$ along the crack front for the CCP specimen.

sion σ. Model dimensions are given in Fig. 9 together with a view of the deformed mesh. The discretization strategy and material properties are the same than for the CCP. For this example 2193 nodes and 407 elements are employed for the domain discretization, while 3198 nodes and 312 cells are used to define the integration domains. Six rings of cells are placed around the crack front for the K computations.

Computed results for K_I are plotted in Fig. 10 and reported in Tables 3 and 4 using the biquadratic and optimised q respectively. The error bar in Fig. 10 indicates the dispersion of the computed results for the point coincident with the free surface when the bi-quadratic function q is used. Following the same format, results for K_{II} are presented in Fig. 11 and reported in Tables 5 and 6. Since results for comparison along the complete crack front are not available for this example, the only value

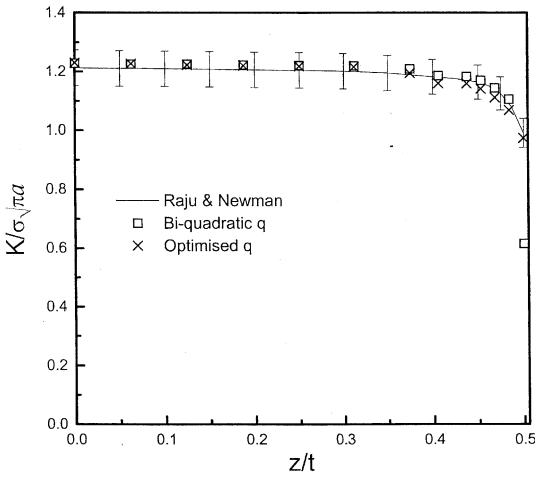

Fig. 8. Variation of $K_I/\sigma\sqrt{\pi a}$ along the crack front for the DENS specimen.

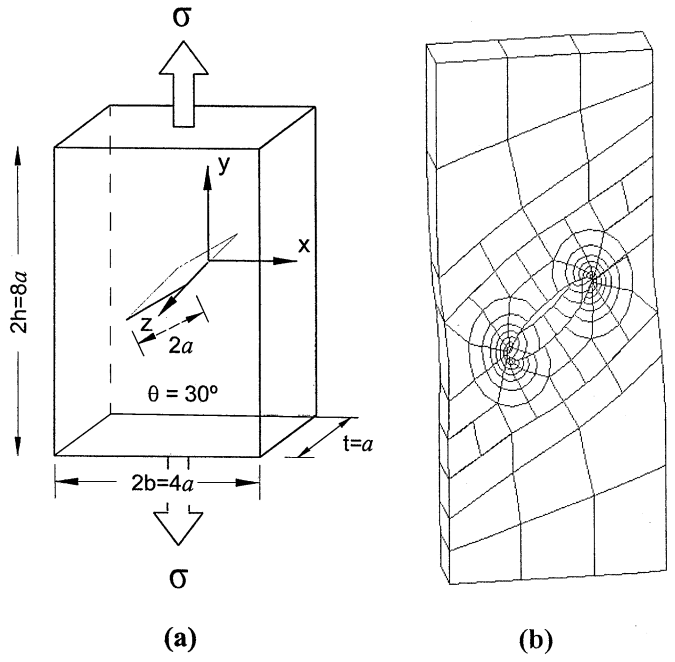

Fig. 9. (a) Schematic with the geometry and dimensions of the thick panel with a center slant crack. (b) Boundary element mesh (deformed).

included as a reference is the plain strain solution due to Kitagawa and Yukki [24] at the specimen mid-plane.

It can be observed that the results show the same behaviour as for the previous example: values obtained using both approaches for the function q are almost coincident along the complete crack front,

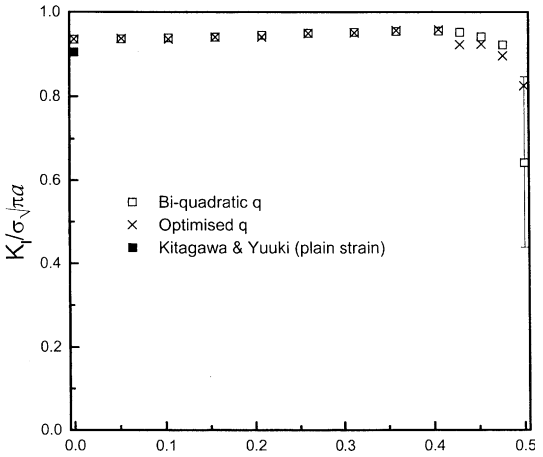

Fig. 10. Variation of $K_1/\sigma\sqrt{\pi a}$ along the crack front for the slant crack.

Table 3
Normalized $K_1/\sigma\sqrt{\pi a}$ results for the slant crack using the bi-quadratic q

z/t	$K_1/\sigma\sqrt{\pi a}$						
	r/a						Average
	0.10	0.17	0.25	0.35	0.50	0.75	
0.0000	0.9268	0.9333	0.9362	0.9376	0.9383	0.9379	0.9350
0.0521	0.9279	0.9341	0.9371	0.9386	0.9394	0.9396	0.9361
0.1042	0.9314	0.9374	0.9399	0.9411	0.9417	0.9421	0.9389
0.1563	0.9327	0.9388	0.9416	0.9431	0.9438	0.9442	0.9407
0.2083	0.9375	0.9436	0.9461	0.9473	0.9479	0.9482	0.9451
0.2604	0.9413	0.9480	0.9510	0.9525	0.9533	0.9536	0.9499
0.3125	0.9451	0.9511	0.9533	0.9543	0.9548	0.9551	0.9523
0.3594	0.9479	0.9534	0.9555	0.9563	0.9567	0.9569	0.9545
0.4063	0.9487	0.9541	0.9561	0.9570	0.9575	0.9579	0.9552
0.4297	0.9466	0.9512	0.9526	0.9532	0.9536	0.9540	0.9519
0.4531	0.9358	0.9408	0.9424	0.9430	0.9432	0.9432	0.9414
0.4766	0.9172	0.9221	0.9236	0.9240	0.9237	0.9228	0.9222
0.5000	0.8133	0.7575	0.6960	0.6264	0.5369	0.4220	0.6420

except at the free surface where the optimised q performs markedly better. Once again K values computed using the bi-quadratic q present a strong dependence with the integration path on the free surface, while the optimised q does not. For the position coincident with the specimen mid-plane, obtained results are in both cases in excellent agreement with the reference value. On the other hand, tabulated results show that K values calculated over the smallest integration domains ($r/a = 0.1$) are more accurate (in what refers to path independence) for the bi-quadratic q. An explanation for this behaviour is that the reduced number of cells in the radial direction of the integration domain (two for the case $r/a = 0.1$), are not able to approximate the optimised function q with the required accuracy. Note that the biquadratic q varies more smoothly than the optimised q (see Fig. 5), and so, it can be accurately approximated using fewer cells. As it is indicated in Tables 4 and 6, results for $r/a = 0.1$ are excluded of the analysis.

Table 4
Normalized $K_I/\sigma\sqrt{\pi a}$ results for the slant crack using the optimised q

z/t	$K_I/\sigma\sqrt{\pi a}$						
	r/a						Average[a]
	0.10	0.17	0.25	0.35	0.50	0.75	
0.0000	0.8977	0.9298	0.9361	0.9372	0.9375	0.9375	0.9356
0.0521	0.9312	0.9372	0.9373	0.9373	0.9373	0.9373	0.9373
0.1042	0.9425	0.9316	0.9366	0.9370	0.9371	0.9371	0.9359
0.1563	0.9339	0.9405	0.9406	0.9406	0.9406	0.9406	0.9406
0.2083	0.9490	0.9364	0.9414	0.9418	0.9419	0.9419	0.9407
0.2604	0.9424	0.9493	0.9494	0.9494	0.9494	0.9494	0.9494
0.3125	0.9485	0.9459	0.9517	0.9522	0.9522	0.9522	0.9509
0.3594	0.9494	0.9564	0.9565	0.9565	0.9565	0.9565	0.9565
0.4063	0.9446	0.9580	0.9582	0.9583	0.9583	0.9583	0.9582
0.4297	0.9215	0.9225	0.9225	0.9225	0.9225	0.9226	0.9225
0.4531	0.9132	0.9237	0.9238	0.9238	0.9238	0.9238	0.9238
0.4766	0.8953	0.8962	0.8962	0.8962	0.8962	0.8962	0.8962
0.5000	0.8423	0.8298	0.8246	0.8236	0.8237	0.8241	0.8252

[a] Average results do not include results obtained for $r/a = 0.1$.

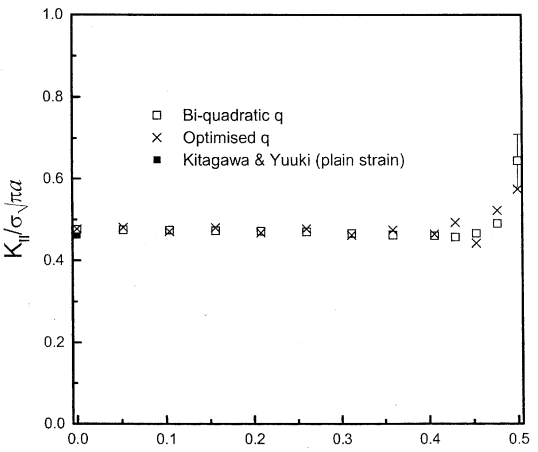

Fig. 11. Variation of $K_{II}/\sigma\sqrt{\pi a}$ along the crack front for the slant crack.

7.3. Thick panel with a central circular arc crack

The last example consists of a thick panel with a central circular arc crack subjected to a uniaxial remote tension σ. Model dimensions are given in Fig. 12, where a view of the deformed mesh is also included. Model boundary discretization is constructed using 425 elements and 2263 nodes, while 312 cells and 3198 nodes are employed to define the integration domains. The discretization strategy and material properties are chosen the same to the previous examples.

Computed results for K_I are plotted in Fig. 13 and reported in Tables 7 and 8 using both approaches for the specification of the function q. The error bar in Fig. 13 indicates the dispersion of the computed results for the point coincident with the free surface when the biquadratic function

Table 5
Normalized $K_{II}/\sigma\sqrt{\pi a}$ results for the slant crack using the bi-quadratic q

z/t	$K_{II}/\sigma\sqrt{\pi a}$						
	r/a						Average
	0.10	0.17	0.25	0.35	0.50	0.75	
0.0000	0.4720	0.4742	0.4755	0.4764	0.4771	0.4785	0.4756
0.0521	0.4723	0.4732	0.4745	0.4756	0.4764	0.4773	0.4749
0.1042	0.4711	0.4725	0.4738	0.4748	0.4754	0.4758	0.4739
0.1563	0.4705	0.4710	0.4724	0.4735	0.4742	0.4744	0.4727
0.2083	0.4686	0.4700	0.4713	0.4723	0.4728	0.4730	0.4713
0.2604	0.4679	0.4686	0.4700	0.4711	0.4718	0.4720	0.4702
0.3125	0.4638	0.4650	0.4661	0.4668	0.4672	0.4672	0.4660
0.3594	0.4603	0.4609	0.4618	0.4624	0.4627	0.4626	0.4618
0.4063	0.4586	0.4595	0.4602	0.4606	0.4606	0.4605	0.4600
0.4297	0.4554	0.4562	0.4566	0.4567	0.4566	0.4565	0.4563
0.4531	0.4636	0.4643	0.4649	0.4656	0.4667	0.4693	0.4657
0.4766	0.4824	0.4842	0.4859	0.4884	0.4928	0.5023	0.4893
0.5000	0.5791	0.6172	0.6467	0.6694	0.6827	0.6684	0.6439

Table 6
Normalized $K_{II}/\sigma\sqrt{\pi a}$ results for the slant crack using the optimised q

z/t	$K_{II}/\sigma\sqrt{\pi a}$						
	r/a						Average[a]
	0.10	0.17	0.25	0.35	0.50	0.75	
0.0000	0.4643	0.4766	0.4766	0.4768	0.4770	0.4771	0.4768
0.0521	0.4872	0.4808	0.4808	0.4808	0.4808	0.4808	0.4808
0.1042	0.4848	0.4689	0.4711	0.4711	0.4712	0.4712	0.4707
0.1563	0.4869	0.4796	0.4796	0.4796	0.4796	0.4796	0.4796
0.2083	0.4803	0.4663	0.4679	0.4679	0.4680	0.4680	0.4676
0.2604	0.4842	0.4770	0.4770	0.4770	0.4770	0.4770	0.4770
0.3125	0.4708	0.4616	0.4617	0.4617	0.4618	0.4618	0.4617
0.3594	0.4798	0.4737	0.4737	0.4737	0.4737	0.4737	0.4737
0.4063	0.4722	0.4641	0.4635	0.4635	0.4635	0.4635	0.4636
0.4297	0.4925	0.4923	0.4923	0.4923	0.4923	0.4923	0.4923
0.4531	0.4416	0.4418	0.4416	0.4416	0.4416	0.4416	0.4417
0.4766	0.5215	0.5213	0.5213	0.5213	0.5213	0.5214	0.5213
0.5000	0.5626	0.5703	0.5737	0.5748	0.5752	0.5754	0.5739

[a] Average results do not include results obtained for $r/a = 0.1$.

q is used. Following the same format, results for K_{II} are presented in Fig. 14 and reported in Tables 9 and 10. The reference values included in the figures for the position coincident with specimen mid-plane were computed using a high-resolution two-dimensional DBEM models under plain strain conditions.

As it happened with the previous examples results show that the optimised q performs markedly better for the point coincident with the free surface, allowing to obtain reliable K values. Once again K values calculated using the smallest integration domains ($r/a = 0.1$) are more accurate (in what refers to path independence) when computed using the bi-quadratic q.

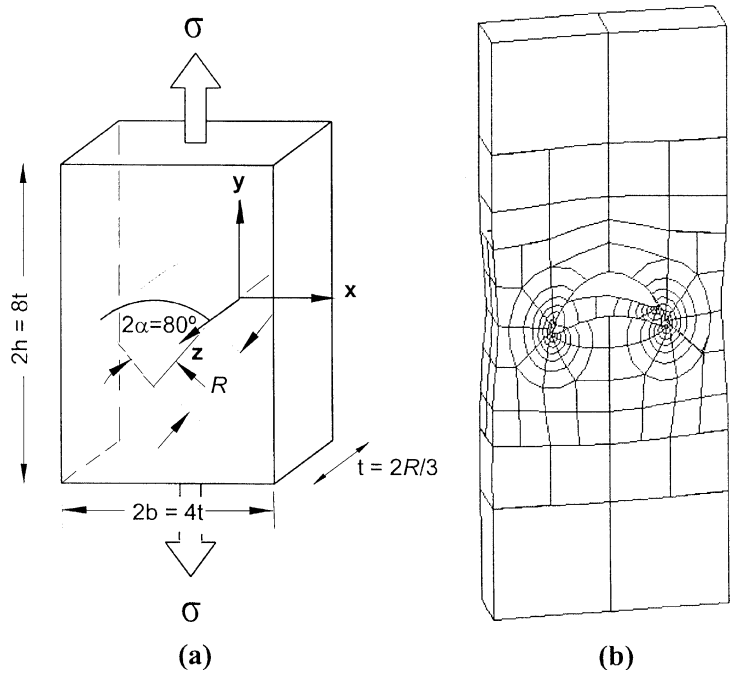

Fig. 12. (a) Schematic with the geometry and dimensions of the thick panel with the circular are crack. (b) Boundary element mesh (deformed).

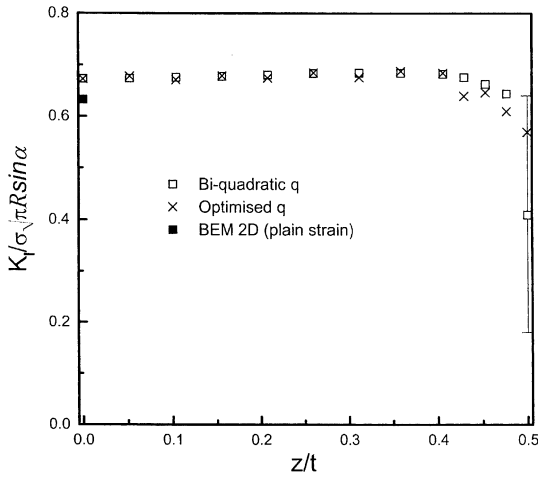

Fig. 13. Variation of $K_1/\sigma\sqrt{\pi a}$ along the crack front for the circular are crack.

It can be also observed from Figs. 13 and 14 that results computed using the bi-quadratic q show a smooth variation along the crack front, while those computed using the optimised q display a rather noisy behaviour of around 3% the reference value. Note that results computed at corner and surface nodes (i.e.

Table 7
Normalized $K_I/\sigma\sqrt{\pi R}\cdot\sin\alpha$ results for the circular arc crack using the bi-quadratic q

z/t	$K_I/\sigma\sqrt{\pi R}\cdot\sin\alpha$						
	r/a						Average
	0.10	0.17	0.25	0.35	0.50	0.75	
0.0000	0.6691	0.6727	0.6748	0.6768	0.6767	0.6679	0.6730
0.0521	0.6687	0.6733	0.6757	0.6781	0.6781	0.6697	0.6739
0.1042	0.6704	0.6754	0.6778	0.6801	0.6802	0.6722	0.6760
0.1563	0.6715	0.6766	0.6792	0.6817	0.6820	0.6742	0.6775
0.2083	0.6746	0.6797	0.6821	0.6845	0.6848	0.6771	0.6805
0.2604	0.6772	0.6827	0.6853	0.6879	0.6882	0.6807	0.6837
0.3125	0.6787	0.6837	0.6859	0.6882	0.6884	0.6810	0.6843
0.3594	0.6791	0.6839	0.6860	0.6881	0.6882	0.6808	0.6844
0.4063	0.6772	0.6819	0.6840	0.6861	0.6861	0.6785	0.6823
0.4297	0.6716	0.6758	0.6774	0.6792	0.6788	0.6704	0.6756
0.4531	0.6593	0.6636	0.6653	0.6666	0.6654	0.6561	0.6627
0.4766	0.6419	0.6455	0.6468	0.6472	0.6449	0.6355	0.6436
0.5000	0.5627	0.5180	0.4681	0.4078	0.3204	0.1804	0.4096

Table 8
Normalized $K_I/\sigma\sqrt{\pi R}\cdot\sin\alpha$ results for the circular are crack using the optimised q

z/t	$K_I/\sigma\sqrt{\pi R}\cdot\sin\alpha$						
	r/a						Average[a]
	0.10	0.17	0.25	0.35	0.50	0.75	
0.0000	0.6409	0.6587	0.6752	0.6771	0.6766	0.6738	0.6723
0.0521	0.6707	0.6776	0.6777	0.6778	0.6777	0.6775	0.6777
0.1042	0.6726	0.6662	0.6717	0.6724	0.6724	0.6721	0.6710
0.1563	0.6711	0.6789	0.6790	0.6790	0.6790	0.6786	0.6789
0.2083	0.6784	0.6700	0.6750	0.6757	0.6757	0.6753	0.6743
0.2604	0.6768	0.6846	0.6848	0.6848	0.6848	0.6842	0.6846
0.3125	0.6828	0.6719	0.6760	0.6766	0.6766	0.6760	0.6755
0.3594	0.6798	0.6877	0.6878	0.6878	0.6878	0.6871	0.6877
0.4063	0.6610	0.6835	0.6842	0.6843	0.6843	0.6835	0.6839
0.4297	0.6383	0.6391	0.6391	0.6391	0.6391	0.6381	0.6389
0.4531	0.6346	0.6464	0.6464	0.6464	0.6464	0.6454	0.6462
0.4766	0.6085	0.6092	0.6092	0.6092	0.6092	0.6081	0.6090
0.5000	0.5806	0.5732	0.5690	0.5677	0.5673	0.5659	0.5686

[a] Average results do not include results obtained for $r/a = 0.1$.

those reported at odd positions in the figures) are almost coincident for the bi-quadratic and the optimised q, while results for mid-side nodes (even positions in the figure) obtained using the optimised q deviate from the general trend. Once again it is argued that the cause of this behaviour is related to a lack of accuracy in the approximation of the optimised q, which exhibits a stronger variation than the bi-quadratic q. Note that in the case of mid-side nodes, the integration volumes V are one-element thick, and so the variation of q in the direction of x_3^* is just approximated within one cell (see Fig. 3). On the other hand for the case of corner nodes, the integration volumes V are two-element thick and so a better approximation of q in the direction of x_3^* is achieved.

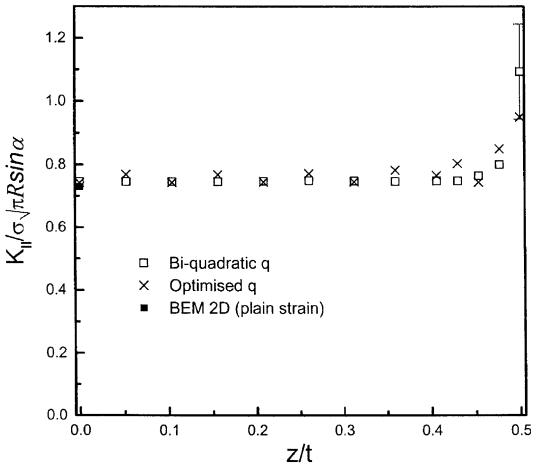

Fig. 14. Variation $K_{II}/\sigma\sqrt{\pi a}$ along the crack front for the circular arc crack.

Table 9
Normalized $K_{II}/\sigma\sqrt{\pi R}\cdot\sin\alpha$ results for the circular are crack using the bi-quadratic q

z/t	$K_{II}/\sigma\sqrt{\pi R}\cdot\sin\alpha$						
	r/a						Average
	0.10	0.17	0.25	0.35	0.50	0.75	
0.0000	0.7483	0.7466	0.7477	0.7372	0.7412	0.7575	0.7464
0.0521	0.7481	0.7466	0.7481	0.7376	0.7413	0.7568	0.7464
0.1042	0.7477	0.7477	0.7493	0.7383	0.7415	0.7561	0.7468
0.1563	0.7485	0.7476	0.7491	0.7382	0.7412	0.7554	0.7467
0.2083	0.7491	0.7492	0.7507	0.7394	0.7421	0.7560	0.7478
0.2604	0.7517	0.7509	0.7524	0.7410	0.7437	0.7573	0.7495
0.3125	0.7504	0.7502	0.7513	0.7394	0.7417	0.7549	0.7480
0.3594	0.7505	0.7495	0.7503	0.7383	0.7404	0.7533	0.7470
0.4063	0.7514	0.7507	0.7513	0.7392	0.7414	0.7544	0.7481
0.4297	0.7515	0.7508	0.7510	0.7392	0.7418	0.7549	0.7482
0.4531	0.7669	0.7656	0.7658	0.7551	0.7595	0.7751	0.7647
0.4766	0.7984	0.7971	0.7981	0.7897	0.7975	0.8197	0.8001
0.5000	0.9587	1.0187	1.0694	1.1074	1.1652	1.2408	1.0934

8. Conclusions

A three-dimensional BEM domain formulation of the M_1-integral methodology for the numerical computation of mixed-mode stress intensity factors has been presented in this paper. The proposed formulation has been implemented as a post-processing technique, and so it can be applied to the results from a particular model at a later stage. The implementation takes advantage of the efficiency of the boundary integral equation to directly obtain the required displacement derivatives, stress and strain fields.

Special emphasis has been put in the appropriate selection of the auxiliary function q present in the domain integral formulation. In this sense two approaches have been considered: a bi-quadratic variation, and an optimised approach recently proposed in the paper by Saliva et al. [9]. A number of examples demonstrate the efficiency and accuracy of the proposed formulation.

Table 10
Normalized $K_{II}/\sigma\sqrt{\pi R}\cdot\sin\alpha$ results for the circular arc crack using the optimised q

z/t	$K_{II}/\sigma\sqrt{\pi R}\cdot\sin\alpha$						
	r/a						Average[a]
	0.10	0.17	0.25	0.35	0.50	0.75	
0.0000	0.7244	0.7381	0.7482	0.7379	0.7418	0.7454	0.7423
0.0521	0.7740	0.7685	0.7685	0.7684	0.7685	0.7687	0.7685
0.1042	0.7615	0.7419	0.7441	0.7436	0.7436	0.7436	0.7433
0.1563	0.7745	0.7684	0.7684	0.7683	0.7684	0.7685	0.7684
0.2083	0.7619	0.7432	0.7454	0.7449	0.7449	0.7450	0.7447
0.2604	0.7778	0.7717	0.7716	0.7716	0.7717	0.7718	0.7717
0.3125	0.7588	0.7452	0.7460	0.7456	0.7456	0.7456	0.7456
0.3594	0.7878	0.7827	0.7826	0.7826	0.7827	0.7828	0.7827
0.4063	0.7634	0.7659	0.7650	0.7650	0.7650	0.7651	0.7652
0.4297	0.8036	0.8034	0.8034	0.8033	0.8035	0.8036	0.8034
0.4531	0.7316	0.7438	0.7433	0.7433	0.7434	0.7436	0.7435
0.4766	0.8500	0.8499	0.8499	0.8498	0.8501	0.8503	0.8500
0.5000	0.9286	0.9428	0.9489	0.9514	0.9528	0.9536	0.9499

[a] Average results do not include results obtained for $r/a = 0.1$.

It has been found that the function q constitutes a key feature for the performance of the proposed methodology. Obtained results show that the optimised q performs markedly better for the point located at the intersection of the crack front with the free surface, allowing obtaining reliable K results where the bi-quadratic q fails. On the other hand, for crack front positions located in the interior of the specimen both approaches allow computing accurate K results, however the bi-quadratic q presents a more robust behaviour. It is observed that, in general, the bi-quadratic q performs better for the integration volumes defined closer to the crack front, and it is also not affected by the number of cells used to define the integration volume in the direction tangent to the crack front.

Acknowledgements

This work was financed by grant PICT 12-12528 of Agencia Nacional de Promoción Científica de la República Argentina.

References

[1] M.H. Aliabadi, D.P. Rooke, Numerical Fracture Mechanics, Computational Mechanics Publications and Kluwer Academic Publishers, Dordrecht and Southampton, 1992.
[2] T.L. Anderson, Fracture Mechanics, Fundamentals and Applications, CRC Press, Boca Ratón, 1995.
[3] J.R. Rice, A path independent integral and the approximate analysis of strain concentration by notches and cracks, J. Appl. Mech., Trans. ASME (1968) 379–386.
[4] T.K. Hellen, On the method of virtual crack extensions, Int. J. Numer. Methods Engrg. (1975) 187–207.
[5] D.M. Parks, A stiffness derivative finite element technique for determination of elastic crack tip stress intensity factors, Int. J. Fract. (1974) 487–502.
[6] W.C. Carpenter, D.T. Read, R.H. Dodds, Comparison of several path independent integrals including plasticity effects, Int. J. Fract. (1986) 303–323.
[7] B. Moran, C.F. Shih, A general treatment of crack tip contour integrals, Int. J. Fract. (1987) 295–310.
[8] G.P. Nikishkov, S.N. Atluri, Calculation of fracture mechanics parameters for an arbitrary three-dimensional crack by the equivalent domain integral method, Int. J. Numer. Methods Engrg. (1987) 1801–1821.

[9] R. Saliva, M.J. Vénere, C. Padra, E. Taroco, R.A. Feijoo, Shape sensitivity analysis and energy release rate of planar cracks embedded in three-dimensional bodies, Comput. Methods Appl. Mech. Engrg. 188 (2000) 649–664.
[10] R.H. Rigby, M.H. Aliabadi, Mixed-mode *J*-integral method for analysis of 3D fracture problems using BEM, Engrg. Anal. Boundary Elements (1993) 239–256.
[11] O. Huber, G. Kuhn, Evaluation of the *J*-integral for 3D crack problems using the hypersingular identity, in: C.A. Brebbia et al. (Eds.), Boundary Elements XIV, CMP Publications, 1992, pp. 367–382.
[12] A.P. Cisilino, M.H. Aliabadi, J.L. Otegui, Energy domain integral applied to solve center and double-edge crack problems in three-dimensions, Theor. Appl. Fract. Mech. 29 (1998) 181–194.
[13] A.P. Cisilino, M.H. Aliabadi, BEM implementation of the energy domain integral for the elastoplastic analysis of 3D fracture problems, Int. J. Fract. 96 (1999) 229–245.
[14] dell'Erba, M.H. Aliabadi, BEM analysis of fracture problems in three-dimensional thermoelasticity using *J*-integral, Int. J. Solids Struct. 38 (2001) 4609–4630.
[15] F.Z. Li, C.F. Shih, A. Needleman, A comparison of methods for calculating energy release rates, Engrg. Fract. Mech. 21 (1985) 405–421.
[16] R. Nathta, B. Moran, Domain integrals for axisymmetric interface crack problems, Int. J. Solids Struct. 30/15 (1993) 2027–2040.
[17] F.H.K. Chen, R.T. Shield, Conservation laws in elasticity of the *J*-integral type, J. Appl. Math. Phys. (ZAMP) 28 (1977) 1–22.
[18] N. Miyazaki, T. Ikeda, T. Soda, T. Munakata, Stress intensity factor analysis of interface crack using boundary element method—Application of contour-integral method, Engrg. Fract. Mech. 45/5 (1993) 599–610.
[19] M. Gosz, J. Dolbow, B. Moran, Domain integral formulation for stress intensity factor computation along curved three-dimensional interface cracks, Int. J. Solids Struct. 35/15 (1998) 1763–1783.
[20] A.P. Cisilino, M.H. Aliabadi, Three-dimensional BEM analysis for fatigue crack growth in welded components, Int. J. Pressure Vessels Piping 70 (1997) 135–144.
[21] A.P. Cisilino, Linear and Non Linear Crack Growth using Boundary Elements, Serie Topics in Engineering, Computational Mechanics Publications, Boston, USA and Southampton, UK, 2000.
[22] C.F. Shih, B. Moran, T. Nakamura, Energy release rate along a three-dimensional crack front in a thermally stressed body, Int. J. Fract. 30 (1986) 79–102.
[23] I.S. Raju, Newman, Three-dimensional finite element analysis of finite-thickness fracture mechanics, Technical Report NASA TN D-8414, 1977.
[24] H. Kitagawa, R. Yuuki, Analysis of arbitrarily shaped crack in a finite plate using conformal mapping, 1st Report—Construction of analysis procedure and its applicability, Trans. Jpn. Soc. Mech. Engrs. 43 (1977) 4354.